JBC RESEARCH ARTICLE

High-speed AFM imaging reveals DNA capture and loop extrusion dynamics by cohesin-NIPBL

Received for publication, February 9, 2023, and in revised form, August 24, 2023 Published, Papers in Press, September 28, 2023,
https://doi.org/10.1016/j.jbc.2023.105296

Parminder Kaur[1,2,*], Xiaotong Lu[3], Qi Xu[4,5], Elizabeth Marie Irvin[6], Colette Pappas[7], Hongshan Zhang[8], Ilya J. Finkelstein[8], Zhubing Shi[4,5], Yizhi Jane Tao[3], Hongtao Yu[4,5], and Hong Wang[1,2,6,*]

From the [1]Physics Department, North Carolina State University, Raleigh, North Carolina, USA; [2]Center for Human Health and the Environment, North Carolina State University, Raleigh, North Carolina, USA; [3]Department of BioSciences, Rice University, Houston, Texas, USA; [4]Westlake Laboratory of Life Sciences and Biomedicine, and [5]School of Life Sciences, Westlake University, Hangzhou, Zhejiang Province, P.R. China; [6]Toxicology Program, and [7]Department of Biological Sciences, North Carolina State University, Raleigh, North Carolina, USA; [8]Department of Molecular Biosciences, University of Texas at Austin, Austin, Texas, USA.

Reviewed by members of the JBC Editorial Board. Edited by Patrick Sung

3D chromatin organization plays a critical role in regulating gene expression, DNA replication, recombination, and repair. While initially discovered for its role in sister chromatid cohesion, emerging evidence suggests that the cohesin complex (SMC1, SMC3, RAD21, and SA1/SA2), facilitated by NIPBL, mediates topologically associating domains and chromatin loops through DNA loop extrusion. However, information on how conformational changes of cohesin-NIPBL drive its loading onto DNA, initiation, and growth of DNA loops is still lacking. In this study, high-speed atomic force microscopy imaging reveals that cohesin-NIPBL captures DNA through arm extension, assisted by feet (shorter protrusions), and followed by transfer of DNA to its lower compartment (SMC heads, RAD21, SA1, and NIPBL). While binding at the lower compartment, arm extension leads to the capture of a second DNA segment and the initiation of a DNA loop that is independent of ATP hydrolysis. The feet are likely contributed by the C-terminal domains of SA1 and NIPBL and can transiently bind to DNA to facilitate the loading of the cohesin complex onto DNA. Furthermore, high-speed atomic force microscopy imaging reveals distinct forward and reverse DNA loop extrusion steps by cohesin-NIPBL. These results advance our understanding of cohesin by establishing direct experimental evidence for a multistep DNA-binding mechanism mediated by dynamic protein conformational changes.

Large-scale spatial segregation of open and closed chromatin compartments and topologically associating domains (TADs), sub-TADs, and loops fold the genome in interphase (1–5). TADs that contain continuous regions of enriched contact frequencies play essential roles in the timing of DNA replication (6), regulation of enhancer-promoter contacts, gene expression, DNA repair, and recombination (7–10). The structural maintenance of chromosomes (SMC) protein family, including cohesin and condensin complexes, play critical roles in 3D chromatin organization in all living organisms (11–13). The core cohesin complex includes SMC1, SMC3, RAD21^{Scc1}, and SA1/SA2^{Scc3} (human^{yeast}, Fig. 1*A*). SMC proteins (SMC1 and SMC3) form long antiparallel coiled coils (arms), each with a dimerization (hinge) domain at one end and an ABC-type ATPase (head) domain at the other. RAD21^{Scc1} interconnects the head domains. In addition, SA1 and SA2 (STAG1 and STAG2) directly interact with the CCCTC-binding factor (CTCF), a ubiquitous zinc-finger protein that specifically localizes to CTCF-binding sites along the genome (14). Though initially identified as an essential complex to hold sister chromatids together (15), numerous studies demonstrated that cohesin is also crucial in mediating 3D chromatin organization during interphase (16–21). Greater than 80% of long-range looping interactions are mediated by some combinations of cohesin, CTCF, and the mediator complex. Cohesin and CTCF are enriched at TAD boundaries and corner peaks that indicate strong interactions at TAD borders (2, 5). Furthermore, NIPBL significantly stimulates cohesin's DNA binding and ATPase activities (22). RAD21 or NIPBL depletion leads to significantly reduced TADs and corner peaks.

A large body of literature supports a model that cohesin-NIPBL mediates TAD and chromatin loop formation through DNA loop extrusion (23–26). The DNA loop extrusion model posits that cohesin creates DNA loops by actively extruding DNA until they are stabilized by CTCF bound at converging CTCF-binding sites (27, 28). Importantly, single-molecule fluorescence imaging studies, including ours, demonstrated that cohesin-NIPBL is capable of DNA loop extrusion in an ATPase-dependent manner (22, 23). Several unique features of the cohesin-NIPBL structure have implications in its mechanism of action. Cohesin-NIPBL contains DNA-binding sites on multiple subunits with DNA-binding affinities that differ by two orders of magnitudes (25). Previous high-speed atomic force microscopy (HS-AFM) imaging also showed that cohesin and condensin are capable of significant conformational changes. These include SMC ring opening and closing, alignment of the SMC arms, elbow bending, and SMC head engagement and disengagement (25,

* For correspondence: Parminder Kaur, pkaur3@ncsu.edu; Hong Wang, hong_wang@ncsu.edu.

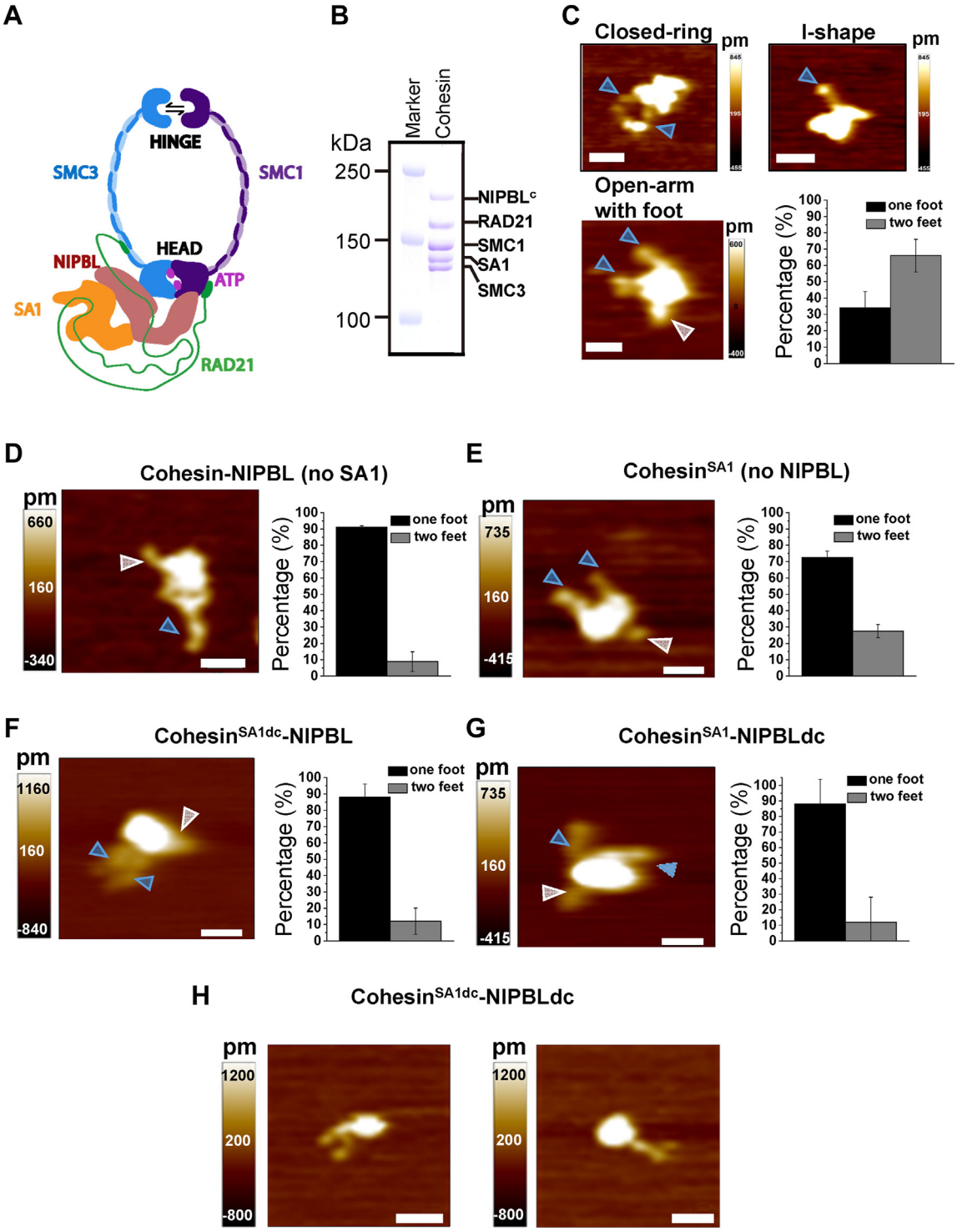

Figure 1. AFM imaging in air shows diverse conformations and foot structures of cohesin-NIPBL. *A*, schematic representation of cohesin^{SA1}-NIPBL based on the cryo-EM structure. *B*, SDS-PAGE of cohesin^{SA1}-NIPBL^{c} showing individual subunits. *C*, example AFM images and analysis of the foot structure of WT cohesin^{SA1}-NIPBL^{c} (N = 50). *D–H*, AFM images (*left* panels) and analysis of the foot structure (*right* panels) on the following: cohesin-NIPBL (*D*, no SA1, N = 114), cohesin^{SA1} (*E*, no NIPBL, N = 142), cohesin^{SA1dc}-NIPBL containing SA1 with C-terminal truncation (*F*, N = 70), cohesin^{SA1}-NIPBLdc containing NIPBL with C-terminal truncation (*G*, N = 85), and example AFM images of cohesin^{SA1dc}-NIPBLdc monomers (*H*). cohesin^{SA1dc}-NIPBLdc monomers were selected using a cut-off molecular weight of 1020 KDa calculated from measured AFM volumes (Kaur *et al.* 2016 https://doi.org/10.1038/srep20513). Scale bar represents 50 nm. The foot structures (*gray arrows*) are identified as the shortest of the protrusions on the same complex, with longer ones as arms (*blue arrows*). N is the number of protein complexes showing foot structures, which are ~40% to 65% of the total complexes analyzed. Each data set was from two to three repeats. Error bars: SD.

29–33). To achieve DNA loop extrusion, cohesin-NIPBL in solution needs first to capture DNA, followed by anchoring onto DNA while still capable of reeling in DNA to enlarge the DNA loop. Observations from single-molecule fluorescence imaging did not provide information on protein conformational changes that drive DNA binding and loop extrusion and

could miss intermediate DNA loop extrusion steps by cohesin (22). Hence, because of technical challenges in studying dynamic multisubunit cohesin–NIPBL complexes, the mechanism of DNA binding and loop extrusion by cohesin is still under intense debate (25, 26, 33–36). Several key questions remain unanswered regarding DNA binding and loop extrusion by cohesin-NIPBL, such as the following: (1) How do each DNA-binding site and protein conformational change contribute to initial DNA binding and loop extrusion? (2) What sequential steps lead to DNA binding and initiation of a DNA loop? (3) What are the DNA loop extrusion step sizes?

Here, we applied traditional AFM imaging in air and HS-AFM imaging in liquids to reveal the structure and dynamics of cohesin-NIPBL–mediated DNA binding and loop extrusion. Our AFM studies show that cohesin-NIPBL uses arm extension to capture DNA and initiate DNA loops independent of ATPase hydrolysis. Surprisingly, foot-like protrusions on cohesin-NIPBL can transiently bind to DNA and facilitate the loading of the cohesin–NIPBL complex onto DNA. Furthermore, HS-AFM imaging reveals distinct forward and reverse DNA loop extrusion steps. These results shed new light on the cohesin-mediated DNA loop extrusion mechanism and provide new directions for future investigation of diverse biological functions of cohesin.

Results

Diverse cohesin-NIPBL conformations and foot structures

Recent studies demonstrated that cohesin-NIPBL contains multiple DNA-binding sites, including the ones on the interface between SMC1 and SMC3 hinges, SMC heads, SA1/SA2 (37), and NIPBL (25). These DNA-binding sites are essential for DNA loop extrusion (25). Despite these new discoveries, our understanding of how each DNA-binding domain on cohesin-NIPBL contributes to cohesin loading onto DNA is limited. To directly address this question, we purified WT cohesin^{SA1}-NIPBL^{c} (Fig. 1*B*) (22, 38), which was shown to be active in DNA loop extrusion and contains SA1 and the C-terminal HEAT repeat domain of NIPBL (22). We applied AFM imaging in air and HS-AFM imaging in liquids (39) to investigate the structure and dynamics of cohesin^{SA1}-NIPBL^{c} alone and in complexes with DNA. Consistent with the previous literature (25), AFM images of the cohesin^{SA1}-NIPBL^{c} collected in the air (+2.5 mM ATP, Fig. 1*C*) showed monomers with SMC arms (blue arrows, Fig. 1*C*) distinguishable from the globular domain, that is, the lower compartment that includes SMC heads, RAD21, SA1, and NIPBL^{c}. Based on their distinct arm features, cohesin^{SA1}-NIPBL^{c} monomers (N_{total} = 127) can be categorized into several classes (Fig. 1*C*), including closed-ring (18.1%), I-shape with closely aligned SMC arms (23.8%), open-arm (21.3%), and those unclassifiable (36.8%). These data suggest that the SMC1/SMC3 hinge interface is highly dynamic, switching between open-arm and closed-ring conformations. Importantly, hinge opening is consistent with the recent discovery of the SMC1/SMC3 hinge interface as one of the DNA entry gates for yeast cohesin (40).

Unexpectedly, in addition to arms, a subpopulation of WT cohesin^{SA1}-NIPBL^{c} molecules (∼40% to 65% from three protein preparations) showed short protrusions (feet). Among cohesin^{SA1}-NIPBL^{c} molecules showing the foot structure, approximately 34.0% displayed one foot and 66.0% displayed two feet (Fig. 1*C*). Relative to arms, the feet were positioned at the opposite side of the globular domain/lower compartment and displayed shorter lengths (25 nm ± 7 nm, N = 50) than the SMC1/SMC3 arms (51 nm ± 15 nm, N = 50). We hypothesized that each cohesin^{SA1}–NIPBL^{c} complex contains two feet, with the possibility of either one or two feet hidden under the globular domain in AFM images. We speculated that the foot structures are the C-terminal domains of SA1 and NIPBL, which were disordered in the cryo-EM structure of cohesin^{SA1}-NIPBL^{c} (38). To test this hypothesis, we imaged five additional complexes, including cohesin-NIPBL^{c} no SA1, cohesin^{SA1} no NIPBL^{c}, cohesin^{SA1dc}-NIPBL (containing SA1 1–1054 AAs without its C terminus), cohesin^{SA1}-NIPBLdc (containing NIPBL1163-2603 AAs without its C terminus), and cohesin^{SA1dc}-NIPBLdc. In AFM images, cohesin-NIPBL^{c} no SA1, cohesin^{SA1} alone no NIPBL^{c}, cohesin^{SA1dc}-NIPBL, and cohesin^{SA1}-NIPBLdc all displayed predominantly one foot (Fig. 1, *D*–*G*). We speculated that the small percentage of cohesin complexes showing two feet without either the SA1/NIPBL subunit or their C-terminal domains might be due to SA1 and NIPBL self-dimerization. Consistent with this hypothesis, while most of SA1dc existed as monomers, a small percentage of molecules displayed AFM volumes greater than SA1dc monomers (Fig. S1, *A* and *B*). For NIPBLdc alone, while the formation of large protein aggregations (∼50% of the total complexes) complicated the interpretation of the results, AFM image analysis also showed complexes displayed AFM volumes greater than NIPBL monomers (Fig. S1*C*). While the biological relevance of higher-order SA1 and NIPBL oligomers is unknown, these results suggest that cohesin^{SA1dc}-NIPBL and cohesin^{SA1}-NIPBLdc showing two feet could be due to the oligomerization of NIPBL and SA1, respectively, in a small population of cohesin complexes *in vitro*. Due to the aggregation of NIPBLdc alone, for cohesin^{SA1dc}-NIPBLdc, we analyzed complexes with globular domain AFM volumes consistent with monomers, based on a previously established standard curve relating AFM volume and molecular weight (41). This analysis revealed that cohesin^{SA1dc}-NIPBLdc predominantly (∼95%, N = 70) showed no foot (Fig. 1*H*). The small percentages of cohesin^{SA1dc}-NIPBLdc molecules showing either one (4%) or two (1%) additional protrusions might be due to arms from oligomerized complexes. In summary, AFM imaging in air shows that foot structures are distinct from SMC1/SMC3 arms and suggests that each C-terminal domain of SA1 and NIPBL contributes to one foot.

A recent study identified three dsDNA-binding patches on SA1, including Patch 1 (K92, K95, K172, and K173), 2 (K555, K558, and R564), and 3 (K969, R971, K1013, and R1016) (25). However, DNA binding by the C-terminal domains of SA1/SA2 and NIPBL, which were disordered in the cryo-EM structure of cohesin-NIPBL (38), has not been investigated. SA1 and SA2 are highly similar, with approximately 70%

sequence identity (42). To further establish DNA-binding domains on SA1/SA2, we purified WT full-length SA2 (1–1231 AAs) and SA2 fragments, including the N-terminal (1–301 AAs or 1–450 AAs) and C-terminal (1052–1231 AAs) domains (Fig. S2*A*) (43). Fluorescence anisotropy measurements using a fluorescently labeled dsDNA substrate (45 bp) revealed that SA2 contains extensive DNA-binding surfaces. Compared to the full-length SA2 (K_d = 63.5 nM ± 1.1 nM), the highest binding affinity is contributed by its N-terminal domain (1–302 AAs: K_d = 110.2 nM ± 7.1 nM; 1–450 AAs: K_d = 55.7 nM ± 0.4 nM) and its C-terminal domain binds to dsDNA weakly (1052–1231 AAs: K_d = 1500.2 nM ± 0.02 nM, Fig. S2, *B–E*). Consistent with these results, we showed previously that deletion of the C-terminal domain of SA2 reduces its binding affinity for dsDNA (44). Thus, these results from fluorescence anisotropy suggest that the C-terminal domain of SA1/SA2 has the potential to bind DNA. Indeed, the C-terminal domain of SA1/SA2 can easily get cleaved during protein purification (43), suggesting that this domain has an extended structure, consistent with the foot-like feature observed in AFM images.

DNA binding and loop initiation by cohesin-NIPBL

To study DNA binding by cohesin-NIPBL, we first employed AFM imaging in air to examine samples of cohesin^{SA1}-NIPBL^{c} and dsDNA (5.19 kb) deposited onto a mica surface (+2.5 mM ATP). Furthermore, to determine if ATPase activity changes DNA-binding modes, we purified the ATP-binding proficient and ATPase-deficient SMC1A-E1157Q/SMC3-E1144Q (EQ) cohesin^{SA1}-NIPBL^{c} mutant. Both WT and ATPase mutant cohesin^{SA1}–NIPBL^{c} complexes were randomly distributed on internal sites along dsDNA (Fig. S3). AFM images revealed different DNA-binding modes by WT cohesin^{SA1}-NIPBL^{c}, as seen previously for condensin (33). WT cohesin^{SA1}-NIPBL^{c} molecules bound to DNA through the arm-hinge (Fig. 2*A*, 30.0% ± 4.1%), the globular domain (53.0% ± 2.1%), both the arm-hinge and globular domains (15.0% ± 2.2%), or the foot (1.9% ± 0.2%). We observed similar DNA-binding modes by the ATPase-deficient EQ cohesin^{SA1}-NIPBL^{c} mutant in AFM images (+ATP, Fig. 2*B*). These results suggest that ATP hydrolysis is not needed for cohesin^{SA1}-NIPBL^{c} loading onto DNA. It is worth noting that a previous AFM study reported DNA binding through the globular and hinge domains of condensin (33).

To further study how cohesin-NIPBL dynamically loads onto DNA and initiates a DNA loop, we applied HS-AFM imaging of WT or ATPase mutant cohesin^{SA1}-NIPBL^{c} in the presence of dsDNA. We recently developed robust sample deposition conditions on a 1-(3-Aminopropyl)silatrane (APS)-treated mica (APS-mica) surface (45). This development enabled us to observe real-time domain protrusion by Twinkle helicase during initial DNA loading (46). We first deposited WT cohesin^{SA1}-NIPBL^{c} (30 nM) with DNA (3 nM, 5.19 kb) onto an APS-mica surface after 16-fold dilution and scanned the sample in a buffer containing ATP (+4 mM ATP) using either a Cypher VRS or JPK NanoWizard HS-AFM at a scan

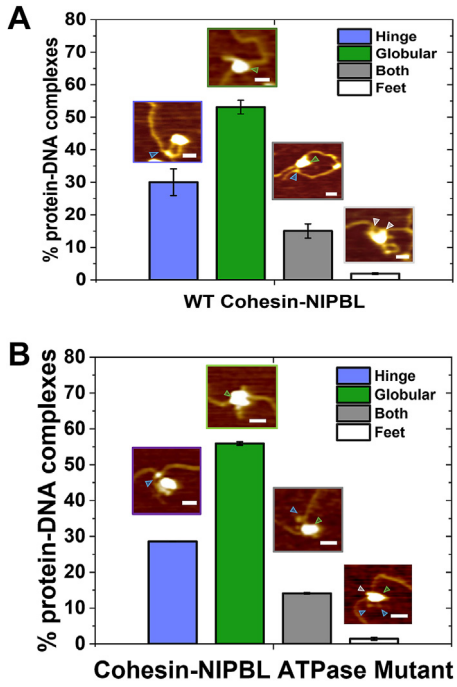

Figure 2. DNA binding by WT and ATPase mutant cohesin-NIPBL revealed by AFM imaging in air. *A* and *B*, percentages of WT (*A*) and ATPase mutant (*B*) cohesin^{SA1}–NIPBL^{c}–DNA complexes with the arm-hinge, globular, both arm-hinge and globular domains, or foot binding to DNA. Inserts: example AFM images of cohesin^{SA1}-NIPBL^{c} binding to DNA. DNA: 5.19 kb; + 2.5 mM ATP. WT cohesin^{SA1}-NIPBL^{c} molecules (N = 105) bound to DNA through the arm-hinge (30.0% ± 4.1%), the globular domain (53.0% ± 2.1%), both the arm-hinge and globular domains (15.0% ± 2.2%), or the foot (1.9% ± 0.2%). The ATPase mutant cohesin^{SA1}–NIPBL^{c} complexes (N = 157) bound to DNA through the arm-hinge (28.6% ± 0.1%), the globular domain (55.9% ± 0.5%), both the arm-hinge and globular domains (14.1% ± 0.2%), or the foot (1.4% ± 0.4%). XY scale bar represents 50 nm. *Blue arrow*: arm; *green arrow*: globular domain; *gray arrow*: foot. At least two independent experiments are performed. Error bars: SD.

rate of 0.4 to 2.3 frames/s. Importantly, under our sample deposition and imaging conditions, both proteins and DNA were mobile on the APS-mica surface. In time-lapse HS-AFM images, cohesin^{SA1}-NIPBL^{c} displayed similar conformations as observed in the static images collected in air (Fig. 1), including I-shape, closed-ring, and folded-arm with some complexes showing protruding feet (Fig. 3*A*). Cohesin^{SA1}-NIPBL^{c} was highly dynamic in the presence of DNA (Fig. 3*B*). Figure 3*B* shows one example of a monomeric WT cohesin^{SA1}-NIPBL^{c} molecule with two arms and a bent elbow extending its arm-hinge domain to capture DNA in proximity (red arrows, Fig. 3*B*). The contact between the hinge domain and DNA was validated in the AFM height profile analysis, which demonstrated the height continuity between the hinge domain and DNA (Fig. S4*A*). Both arms from this cohesin^{SA1}-NIPBL^{c} molecule attempted to capture the DNA nearby (Video S1). Interestingly, a foot was also visible on this cohesin^{SA1}-NIPBL^{c} molecule (gray arrow, Fig. 2*B*), which transiently interacted with the DNA. The foot structure connected to the cohesin-NIPBL can be differentiated from small free particles (likely due to degradations) based on their height profile continuity from the globular domain (Fig. S4, *B* and *C*). In HS-AFM images, approximately 60% of cohesin ^{SA1}-NIPBL^{c} molecules (N = 50) showed either one foot or two feet.

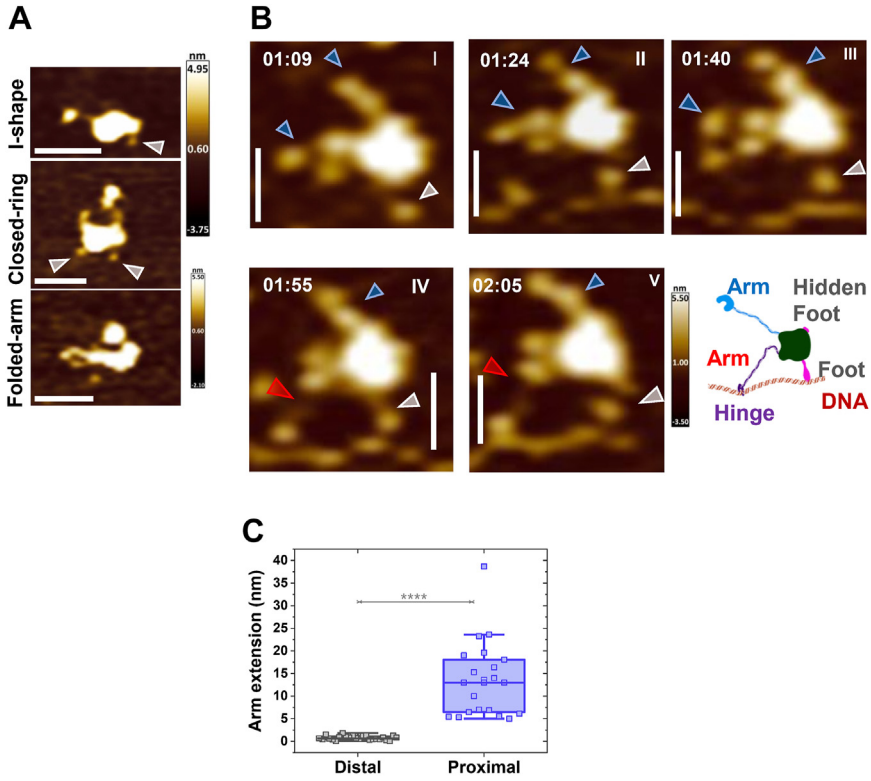

Figure 3. Real-time HS-AFM imaging in liquids reveals that WT cohesin-NIPBL captures DNA through the extension of the arm-hinge domain. *A*, HS-AFM images showing diverse conformations of WT cohesin^{SA1}-NIPBL^{c} in liquids (+4 mM ATP). *B*, DNA capture by the extension of the arm-hinge domain on WT cohesin^{SA1}-NIPBL^{c} (+4 mM ATP). DNA substrate: 5.19 kb. Also see Video S1. *Blue arrow*: arm; *red arrow*: arm extension; *gray arrow*: foot. Time: min:s. XY scale bar represents 50 nm. *C*, box-plot of arm extension lengths for WT cohesin^{SA1}-NIPBL^{c} at a distal (>500 nm distance, N = 24 events) or proximal (<50 nm distance, N = 21 events) location from the DNA. Total: three experiments; 0.4 to 2.3 frame/s. Error bars: SD. **** $p < 10^{-8}$. HS-AFM, high-speed atomic force microscopy.

To investigate whether the presence of DNA drives arm extension, we further analyzed the change in arm lengths measured between consecutive HS-AFM image frames for WT cohesin^{SA1}-NIPBL^{c} when the protein complex was either close to (<50 nm distance) or far from (>500 nm distance) DNA. Strikingly, the arm-hinge extended significantly ($p < 2.5 \times 10^{-9}$) longer for cohesin^{SA1}-NIPBL^{c} proximal to the DNA ($N_{proximal}$ = 21, 13.6 nm ± 8.4 nm) than protein complexes distal to the DNA (N_{distal} = 24, 0.8 nm ± 0.5 nm, Fig. 3*C*).

Furthermore, we observed sequential events showing DNA being captured by the arm-hinge domain, followed by the transfer of DNA to the globular domain on WT cohesin^{SA1}-NIPBL^{c} (Fig. 4 and Video S2). This example in Figure 4 shows a WT cohesin^{SA1}-NIPBL^{c} monomer with a closed-ring configuration that was initially proximal to the DNA (Fig. 4*I*). The DNA was bent while being captured by the arm-hinge domain (Fig. 4*I*) and then transferred to the globular domain (Fig. 4II). During the time interval when DNA was bound to the globular domain, the arm-hinge domains were open and extended out, trying to capture the nearby DNA at the top (red arrow, Fig. 4III) or on the right (red arrow, Fig. 4IV). Notably, two feet were visible in some frames (gray arrows, Fig. 4, *V*, VI, and VII), which appeared to interact with DNA transiently (Fig. 4VI). Finally, a DNA loop was initiated after the capture of the nearby DNA segment by its arm-hinge domain (Fig. 4VII). Transient DNA binding by the foot is a recurring feature observed in HS-AFM imaging for both WT and ATPase mutant cohesin^{SA1}-NIPBL^{c} (N = 14 molecules).

While cohesin^{SA1}-NIPBL^{c} EQ ATPase mutant is expected to retain nucleotide-binding activity, it displays minimal ATPase catalytic activity in the presence of DNA and NIPBL^{c} (22). If initial DNA capture by the cohesin arm-hinge domain depends on ATPase hydrolysis, the cohesin^{SA1}-NIPBL^{c} EQ ATPase mutant would be defective in arm extension. However, the cohesin^{SA1}-NIPBL^{c} ATPase mutant displayed initial DNA capture processes similar to WT cohesin^{SA1}-NIPBL^{c} (Fig. 5). Figure 5*A* shows an example of a cohesin^{SA1}-NIPBL^{c} ATPase mutant monomer with two arms displaying dynamic conformational changes before binding to DNA, including closed-ring and open-arm with bent elbows (Fig. 5*A* and Video S3) (25). Similar to the WT complex, cohesin^{SA1}-NIPBL^{c} ATPase mutant captured DNA through dramatic conformational changes and extension of the arm-hinge domain (red arrows in Fig. 5, *B* and C and Videos S4 and S5). The average length of arm extension for the cohesin^{SA1}-NIPBL^{c} ATPase mutant proximal to the DNA was measured to be 13.2 (±8.6) nm (Fig. 5*D*), comparable to the WT cohesin complex (Fig. 3*C*). Importantly, arm extension events were in random directions relative to the scan direction of the AFM tip. These observations rule out the assumption that arm extension is triggered by AFM tips dragging the protein. Interestingly, HS-AFM imaging revealed diffusion (walking) of the cohesin^{SA1}-

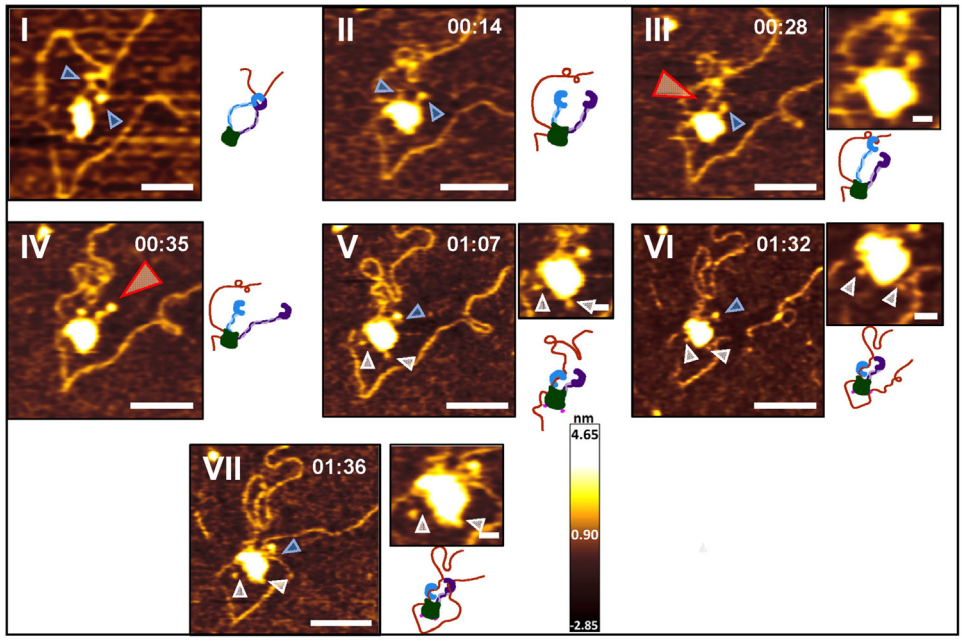

Figure 4. HS-AFM imaging in liquids shows sequential DNA-binding events and the initiation of a DNA loop by WT cohesin-NIPBL. Time-lapse HS-AFM images (*left panels*) and models (*right panels*) showing initial DNA capture by the arm-hinge domain (I), transfer of DNA binding to the globular domain (II), arm extension (III and IV), and the initiation of a DNA loop by the arm-hinge domain on WT cohesin^{SA1}-NIPBL^{c} (VII); + 4 mM ATP. Also see Video S2. Panel I is from an earlier time-lapse series of the same molecule. Images on top of the models: zoomed images. DNA substrate: 5.19 kb. *Blue arrow*: arm; *red arrow*: arm extension; *gray arrow*: foot. Time: min:s. XY scale bar represents 50 nm in large images and represents 10 nm in Zoomed images. HS-AFM, high-speed atomic force microscopy.

NIPBL^{c} ATPase mutant on DNA using short protrusions (Fig. S5 and Videos S3 and S4).

HS-AFM imaging in liquids relies on an intricate balance to keep protein and DNA molecules partially anchored onto a surface while still being mobile. A previous HS-AFM study hinted that a bare mica surface is not suitable for studying the dynamics of DNA binding by cohesin-NIPBL (25). By tuning the APS concentration on a mica surface (45), we were able to

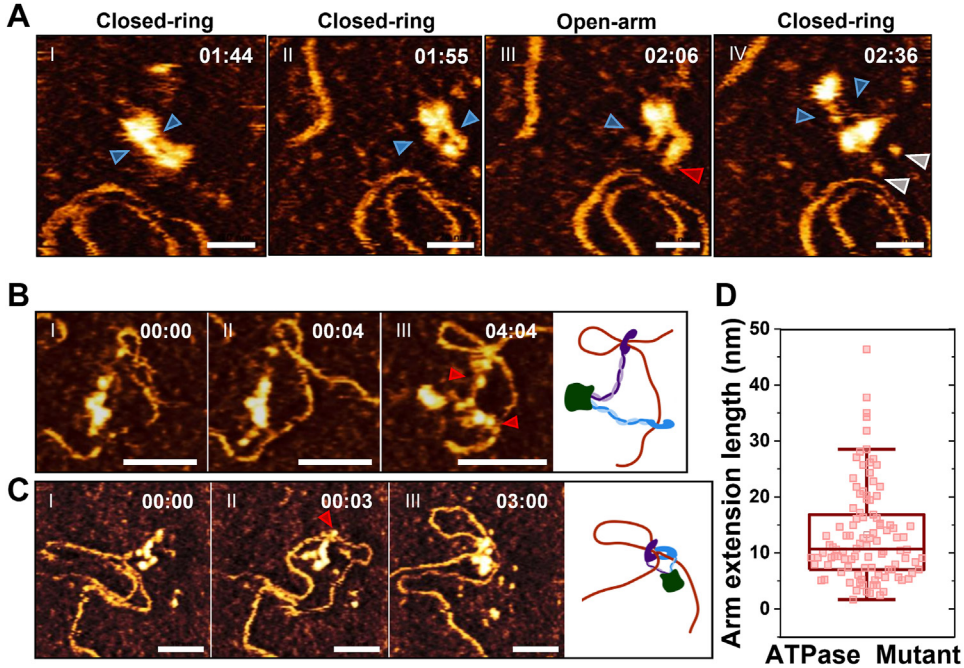

Figure 5. HS-AFM imaging in liquids demonstrates that the cohesin-NIPBL ATPase mutant captures DNA through the extension of the arm-hinge domain. *A*, conformational changes of cohesin^{SA1}-NIPBL^{c} ATPase mutant (Video S3). *B* and *C*, DNA capture through arm extension by the cohesin^{SA1}-NIPBL^{c} ATPase mutant (*B*: Video S4; *C*: Video S5). The buffer contains 4 mM ATP. *Right panels* in *B* and *C*: models. *Blue arrow*: arm; *red arrow*: arm extension; *gray arrow*: foot. XY scale bar represents 50 nm. Time: min:s. *D*, box plot showing arm extension lengths (13.2 nm ± 8.6 nm, N = 102 events) on the cohesin^{SA1}-NIPBL^{c} ATPase mutant at proximal (<50 nm distance) location from DNA. HS-AFM, high-speed atomic force microscopy.

observe cohesin with diverse motion on the surface, from mobile arms to a whole cohesin molecule randomly diffusing on a surface to capture nearby DNA (Fig. 5*A* and Video S3). In summary, HS-AFM imaging might not capture each protein complex's full range of motion and the complete process from DNA loading to loop extrusion. However, by gathering information from HS-AFM images of many dynamic molecules, HS-AFM imaging provides a unique window into sequential events and protein conformational changes during DNA binding. Furthermore, it is worth noting that in HS-AFM images, cohesin^{SA1}-NIPBL^{c} molecules might display transient extra "small domains" on the arms (Fig. 3*B*III) in addition to the previously reported hinge and elbow. These extra "domains" in HS-AFM images are likely due to the dynamic nature of the arms and transient surface anchoring at these regions. In addition, DNA might display missing regions due to temporary detachment from the surface (Fig. 4VI). These features are intrinsic to an "active" complex on an APS-mica surface.

ATPase-independent and ATPase-dependent cohesin-NIPBL mediated DNA looping and bending

HS-AFM imaging shows that both WT and ATPase mutant cohesin^{SA1}-NIPBL^{c} can form DNA loops through diffusion capture of DNA segments in proximity (Figs. 4 and 5). Next, we directly compared the DNA looping efficiency and loop structures mediated by WT and ATPase mutant cohesin^{SA1}-NIPBL^{c}. AFM images (collected in air) of WT (±ATP) and ATPase mutant (+ATP) cohesin^{SA1}-NIPBL^{c} (30 nM) in the presence of dsDNA (5.19 kb, 6 nM) showed distinct protein-mediated DNA loops (Fig. 6). On incubating WT (-ATP) or ATPase mutant cohesin^{SA1}-NIPBL^{c} (+ATP) with the linear dsDNA, 15.6% (±4.3%) and 18.1% (±0.3%) of dsDNA molecules, respectively, contained protein-mediated DNA loops (Fig. 6*B*). For WT cohesin^{SA1}-NIPBL^{c}, the addition of ATP (+2.5 mM ATP) significantly increased ($p < 0.05$) the population of DNA molecules with protein-mediated loops to 65.2% (±3.6%, Fig. 6*B*). Furthermore, AFM imaging revealed cohesin^{SA1}-NIPBL^{c}–mediated nested DNA loops (a loop within a loop, yellow arrows in Fig. 6*A*). Nested DNA loops can be generated when cohesin-NIPBL at an existing DNA loop captures an additional DNA segment (ATPase-independent) or two separate cohesin-NIPBL molecules on the same DNA collide after DNA loop extrusion (ATPase-dependent, Fig. 6*C*) (47). The population of nested DNA loops out of total DNA loops observed for WT cohesin^{SA1}-NIPBL^{c} in the presence of ATP (74.7% ± 4.0%) was significantly ($p < 0.05$) greater than that observed for either WT cohesin^{SA1}-NIPBL^{c} without ATP (32.8% ± 5.9%) or the ATPase mutant (20.6% ± 2.8%, Fig. 6*B*). In comparison, less than 5% of DNA alone (N = 100) without cohesin^{SA1}-NIPBL showed loop structures. This result supported the notion that DNA loops in the presence of cohesin^{SA1}-NIPBL were not due to the capture of existing DNA loops by proteins. Instead, these results collectively suggest that cohesin-NIPBL mediates DNA loops through two distinct mechanisms: ATPase-independent diffusion capture of DNA segments in proximity and ATPase-dependent DNA loop extrusion (Fig. 6*C*). Furthermore, compared to the WT cohesin^{SA1}-NIPBL, the absence of the C-terminal domains of either SA1 or NIPBL significantly reduced the percentage of cohesin^{SA1}-NIPBL–DNA complex binding on DNA (Fig. S6, *A*–*C*). This result suggested that the C-terminal domains of SA1 and NIPBL (the foot structures) directly contribute to the loading of cohesin–NIPBL complex onto DNA. In comparison, the percentages of DNA loops and nested loops were only slightly reduced (Fig. S6, *D* and *E*).

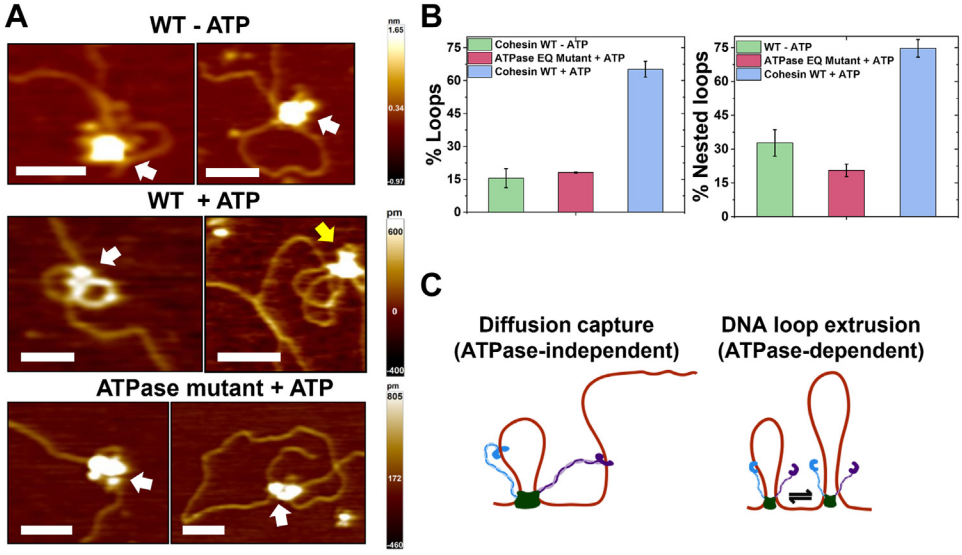

Figure 6. AFM imaging in air reveals cohesin-NIPBL–mediated DNA loops. *A*, representative AFM images of DNA loops mediated by WT cohesin^{SA1}-NIPBL^{c} in the absence (*top*) and presence of ATP (*middle*) and the cohesin^{SA1}-NIPBL^{c} ATPase mutant in the presence of ATP (*bottom*) on linear DNA. Cohesin^{SA1}-NIPBL^{c}: 30 nM; DNA (5.19 kb): 6 nM; ATP: 2.5 mM. *White arrow*: single loop; *Yellow arrow*: nested loop. XY scale bar represents 100 nm. *B*, quantification of the percentages of DNA molecules containing protein-mediated total DNA loops (*left panel*, N = 155 DNA) and nested loops out of total DNA loops (*right panel*). Error bars: SD. Two experiments for each condition. *C*, a model representing mechanisms of ATPase-independent diffusion capture of an additional DNA segment (*left panel*) and ATPase-dependent DNA loop extrusion by cohesin-NIPBL that might lead to nested DNA loops (*right panel*).

In addition to DNA loops, AFM imaging in air revealed cohesin^{SA1}-NIPBL^{c}–induced DNA bending (Fig. S7). While DNA alone showed slight bending (27.5° ± 26.0°, +ATP), WT cohesin^{SA1}-NIPBL^{c} in the absence of ATP (43.7° ± 20.5°) and cohesin^{SA1}-NIPBL^{c} ATPase mutant (+ATP, 47.3° ± 41.0°) induced significantly ($p < 0.05$) higher degrees of DNA bending (Fig. S7, *A–D*). Furthermore, compared to DNA binding by WT cohesin^{SA1}-NIPBL^{c} without ATP, the presence of ATP further augmented ($p < 0.05$) the DNA bending (57.2° ± 27.6°, Fig. S7*D*). Additionally, we compared the DNA bending angles induced by either the globular or the hinge domain. The globular domain on WT and ATPase mutant cohesin^{SA1}-NIPBL^{c} induced comparable DNA bending, which was significantly ($p < 0.05$) higher than what was induced by the hinge domains (Fig. S7*E*). In summary, these results from AFM imaging demonstrate that cohesin-NIPBL bends DNA at different DNA-binding steps, which is independent of ATP hydrolysis and could facilitate DNA looping.

HS-AFM imaging in liquids reveals DNA loop extrusion dynamics by cohesin-NIPBL

AFM imaging in air revealed that WT cohesin^{SA1}-NIPBL^{c} in the presence of ATP induced a higher percentage of DNA loops than the WT protein complex without ATP or the ATPase mutant (Fig. 6). This result is consistent with the notion that WT cohesin^{SA1}-NIPBL^{c} is capable of DNA loop extrusion in an ATP hydrolysis–dependent manner. A recent study using magnetic tweezers with a resolution of ∼10 nm revealed a broad distribution of DNA looping step sizes by condensin (48). We expected that real-time HS-AFM imaging of cohesin^{SA1}-NIPBL^{c} with DNA (+ATP) would directly reveal DNA extrusion steps. Because DNA movement during imaging could contribute to slight DNA length fluctuations without DNA loop extrusion, we first carried out control experiments using HS-AFM imaging to measure DNA loop length changes for the cohesin^{SA1}-NIPBL^{c} ATPase mutant (+ATP, Figs. 7*A* and S8*A*). The DNA loop length changes (step sizes) measured between HS-AFM image frames fluctuated slightly with small forward (increased, 1.2 nm ± 1.1 nm) and reverse (decreased, −1.34 nm ± 1.0 nm) changes (normalized to per second, Fig. 7*B*). In stark contrast, DNA loop lengths mediated by WT cohesin^{SA1}-NIPBL^{c} (+ATP) showed forward and reverse step sizes, significantly higher than the background fluctuation observed for the ATPase mutant (Figs. 7, *C* and *D*, S8*B*, and Videos S6 and S7). Thus, the large DNA loop length changes mediated by WT cohesin^{SA1}-NIPBL^{c} in the presence of ATP were not due to DNA detachment from or reattachment to the APS-mica surface. If this were true, we would obtain comparable DNA loop length changes for WT and the ATPase mutant under the same imaging conditions. In addition, DNA loop expansion events were in random directions relative to the direction of the scan by the AFM tip. These observations rule out artifacts from the scanning tip dragging DNA. The distribution of the DNA looping step size mediated by WT cohesin^{SA1}-NIPBL^{c} greater than the background fluctuation (>5 nm) displayed forward steps at 13.2 nm (±16.1 nm) and reverse steps at −12.0 nm (±9.8 nm, Fig. 7*E*). Collectively, HS-AFM imaging demonstrates active DNA loop extrusion by WT cohesin-NIPBL in the presence of ATP with distinct DNA loop extrusion step sizes. The DNA looping step size measured from HS-AFM images (∼13 nm or 42 bp) for cohesin^{SA1}-NIPBL^{c} is slightly lower than the step size of condensin (∼20–40 nm) under DNA stretching forces from 1 to 0.2 pN (48).

Discussion

While recent single-molecule fluorescence studies demonstrated DNA loop extrusion by cohesin-NIPBL, the mechanisms of DNA capture and DNA loop initiation by cohesin-NIPBL are still under intense debate (49–51). Several competing models have been proposed to explain the steps driving DNA loop extrusion without reaching a consensus. These models include the tethered inchworm (34), DNA-DNA-segment-capture (35), hold-and-feed (52), scrunching (33), “swing” and “clamp” (25), and Brownian ratchet models (26). However, direct experimental evidence to fully support or discriminate against these models is still lacking. We did not directly aim to approve or disapprove certain DNA loop extrusion models. Instead, our main goal was to define the role of cohesin subunits and protein conformational changes in driving DNA binding and loop extrusion initiation.

The crystal structure of the SMC1-SMC3 hinge heterodimer contains a short ssDNA bound to the outer surface of the SMC1 hinge, suggesting its role in DNA binding (38). Previously, we solved two structures of the SMC1/SMC3 hinge heterodimer that adopt different open conformations, suggesting that the interface between SMC1-SMC3 hinges is highly dynamic (38). Furthermore, a recent report from the Nasmyth group showed that yeast cohesin contains two DNA entry gates, one at the SMC3/Scc1 interface and a second one at the SMC1/SMC3 hinge (40). In this study, AFM in air and HS-AFM imaging in liquids establish that cohesin^{SA1}-NIPBL^{c} displays closed-ring and open-arm configurations. These results provide direct experimental evidence that SMC1/SMC3 hinge–hinge interaction is dynamic and can switch between open and closed states. It is worth noting that the length of SMC1/SMC3 arms measured in AFM images collected in the air shows a relatively broad distribution (51 nm ± 15 nm). This is likely due to the bending of the arm at the elbow. Furthermore, HS-AFM imaging in liquids reveals DNA capture by the cohesin arm-hinge domain. Strikingly, HS-AFM imaging shows that the arm-hinge of WT and ATPase mutant cohesin^{SA1}-NIPBL^{c} can extend ∼14 nm to capture DNA in proximity. Since cohesin^{SA1}-NIPBL^{c} ATPase mutant displays the same DNA capture process through the arm-hinge domain as the WT complex, it suggests that arm extension is not directly driven by ATP hydrolysis. The SMC hinge domains contain positively charged patches (25). Likely, the electrostatic interaction between the hinge domain and negatively charged DNA backbone targets the hinge domain to DNA. This model is consistent with previous findings that mutations at three conserved lysine residues on the lumen of the yeast cohesin

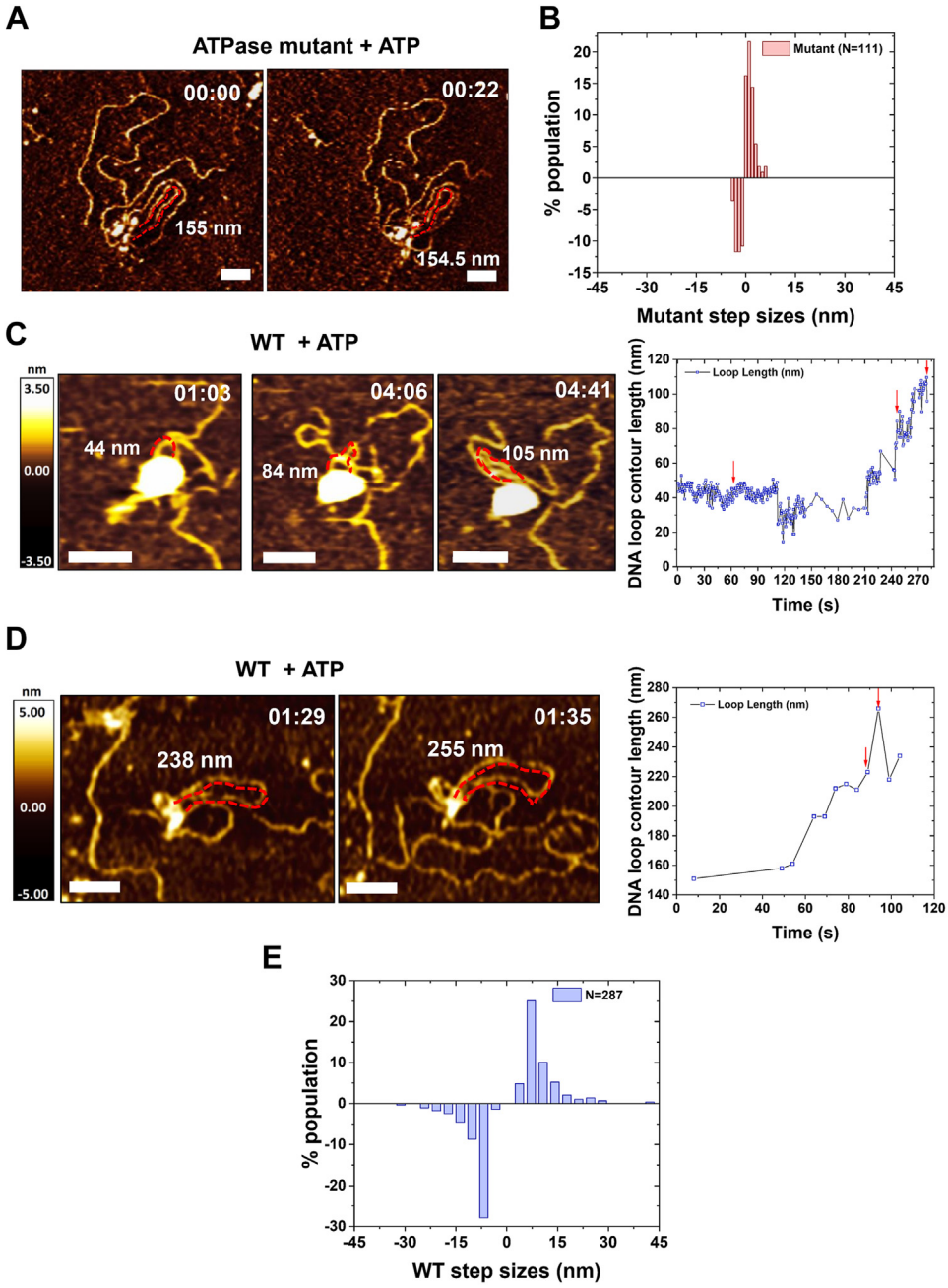

Figure 7. DNA loop extrusion revealed by HS-AFM imaging of cohesin–NIPBL–DNA complexes. *A*, representative time-lapse HS-AFM images of the cohesin^{SA1}-NIPBL^{c} ATPase mutant on a linear dsDNA (5.19 kb) in a buffer containing 4 mM ATP. *B*, histogram of the forward (1.2 nm ± 1.1 nm, N = 60 events) and reverse (−1.34 nm ± 1.0 nm, N = 51 events) DNA loop changes (per second) for ATPase mutant cohesin^{SA1}-NIPBL^{c}, measured based on frame-to-frame loop length changes in HS-AFM images (seven DNA loops). *C* and *D*, *left panels*: time-lapse AFM images showing DNA loop length changes mediated by WT cohesin^{SA1}-NIPBL^{c} on a linear dsDNA (5.19 kb) in a buffer containing 4 mM ATP. *Right panels*: the DNA loop contour lengths over time with the *red arrows* marking the image frames shown in the corresponding *left* panels. Also see Videos S6 and S7. *Dotted red lines* mark the DNA loops and the numbers in nm indicate DNA loop lengths. Time: min:s. XY scale bar represents 50 nm; 1 to 2.3 frames/s. *E*, histogram of the forward (13.2 nm ± 16.1 nm, N = 115 events) and reverse (−12.0 nm ± 9.8 nm, N = 107 events) DNA loop extrusion step size (per second) for WT cohesin^{SA1}-NIPBL^{c} (18 DNA loops, four experiments). Step sizes in panels B and E were collected using the same procedure by measuring DNA loop length changes between HS-AFM image frames. Background fluctuation of DNA length (<5 nm) based on the measurement for the cohesin^{SA1}-NIPBL^{c} ATPase mutant (panel *B*) was excluded in panel *E*. HS-AFM, high-speed atomic force microscopy.

abolished the loading of cohesin onto the chromatin (53). Based on these observations, the Nasmyth group suggested that the positive charges normally hidden inside the SMC hinge's lumen are transiently exposed to DNA through significant conformational changes at the arm-hinge domain (53). Both protein and DNA molecules could be mobile during HS-AFM imaging and their interaction is an intricate "dance". Therefore, there is an uncertainty in using HS-AFM to determine the precise distance between cohesin and DNA that activates arm extension through electrostatic interactions. It is worth noting that in coarse-grained molecular dynamics modeling based on the Debye-Huckel theory, the cutoff

distance for electrostatic interactions between proteins and DNA is typically at ~3 to 5 nm for an ionic concentration of 150 mM (54–56).

Consistent with previous studies (25), in our AFM images, SMC1 and SMC3 heads, RAD21, SA1, and NIPBL^{c} (lower compartment) collectively show up as a globular domain. DNA-binding surfaces on these subunits have been revealed by cryo-EM structures of cohesin^{SA1}-NIPBL^{c} and DNA-binding assays (25, 38). Upon initial DNA binding through the SMC arm-hinge domain, DNA is transferred to the globular domain (Fig. 4), for which our recent cryo-EM structure of cohesin^{SA1}-NIPBL^{c} provides additional detail on DNA binding (38). Specifically, this structure showed that cohesin^{SA1}-NIPBL^{c} binds DNA at the top of the engaged SMC1/SMC3 heads with NIPBL and SA1 wrapping around DNA, creating a central channel (38). It was suggested that ATP binding opens the head gate to complete the DNA entry, and head engagement leads to a DNA "gripping/clamping" state (51). Results from HS-AFM imaging from this study do not contradict this model. Instead, observations from this study support a comprehensive model in which transient DNA binding by the arm-hinge precedes the DNA "gripping/clamping" state at the globular domain (Fig. 8). Our AFM and previously reported studies revealed that cohesin adopts multiple conformations, including the closed ring, I-shaped rod and folded state. In our previous cryo-EM structure of cohesin-NIPBL–DNA complex in the DNA loading or gripping state (38), the hinge directly contacts SA1 and is close to NIPBL. This structure indicates that the hinge after the initial DNA binding can reach the global domain following the bending of coiled-coils. Two DNA entry gates, the hinge and the SMC3–RAD21 interface, have been proposed (40, 51). Consistent with these previous observations, we propose two possible pathways for DNA entry after the initial hinge-DNA contact. In our previous cryo-EM structure, the hinge is partially opened in one of two interfaces. This may either allow DNA entrance into the cohesin ring once the hinge is fully opened or DNA release, followed by the transfer of DNA to SA1 and/or NIPBL that are close to the hinge in the DNA loading or gripping state. In the latter case, when DNA is transiently detached from the hinge domain, stronger electrostatic interactions between the DNA and the globular domain (supported by positively charged surfaces on SMC heads, SA1, and NIPBL) will attract DNA to it. It is worth noting that NIPBL in the complex is adjacent to the SMC3-RAD21 gate and may enable the stabilization of DNA to the globular domain after passing this gate.

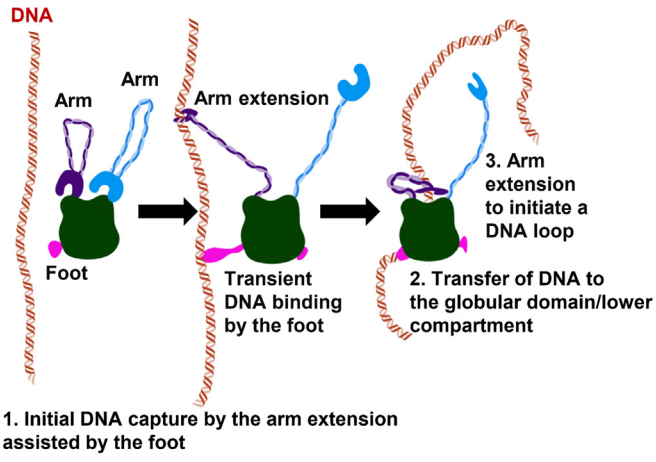

Figure 8. Multistep DNA binding and loop initiation model for cohesin-NIPBL. DNA capture by arm extension followed by transferring of DNA to the globular domain in an ATPase-independent manner. While not shown in the diagram, the SMC1/SMC3 arm-hinge is dynamic and capable of switching between the closed-ring and open-arm configurations. SMC, structural maintenance of chromosome.

Unexpectedly, in addition to arms, some cohesin^{SA1}-NIPBL^{c} molecules display short protrusions (feet) from the globular domain. We also observed a random walk of cohesin^{SA1}-NIPBL^{c} on DNA through short protrusions (likely feet), possibly driven by thermal energy (Fig. S5 and Video S3) (Fig. S3 and Video S3). The presence of DNA-binding foot structures on cohesin^{SA1}-NIPBL^{c} is supported by the following: (1) both AFM imaging in air and HS-AFM imaging in liquids show that foot structures are unique in length compared to the SMC1/SMC3 arms; (2) cohesin-NIPBL without either SA1, NIPBL, or the C-terminal domains of SA1/NIPBL displays predominantly one foot; (3) foot structures transiently bind to DNA and contribute to the formation of cohesin-NIPBL–DNA complex; (4) the C-terminal domain of SA2 (1051–1231 AAs) directly binds to DNA. Furthermore, sequence alignment shows that the C-terminal domain of NIPBL contains numerous conserved positively charged residues (Fig. S9). Thus, we argue that the feet structures are likely the C-terminal domains of SA1 and NIPBL (~200 AAs), which were unstructured in the cohesin^{SA1}-NIPBL^{c} cryo-EM structures (38).

Importantly, AFM imaging of cohesin–NIPBL complexes from this study demonstrates that cohesin-NIPBL promotes DNA looping through two distinct mechanisms. WT cohesin^{SA1}-NIPBL^{c} without ATP and the ATPase mutant are both capable of capturing DNA loops. These results show that cohesin-NIPBL can sequentially capture two DNA segments in proximity through Brownian motion (diffusion capture) independent of ATP hydrolysis. Secondly, WT cohesin^{SA1}-NIPBL^{c} in the presence of ATP further increases the percentage of DNA molecules displaying loops and nested loops, likely through ATPase-dependent DNA loop extrusion (Fig. 6*C*). Multiple previous studies strongly support the physiological relevance of ATPase-independent DNA loops mediated by SMC family proteins: (1) when cohesin is depleted and resupplied to human cells, small and large DNA loops can form with similar dynamics, which is more consistent with diffusion capture than gradual ATPase-dependent DNA loop growth (57); (2) molecular dynamics simulations demonstrated that a combination of diffusion capture and loop extrusion recapitulates condensin-dependent mitotic chromatin contact changes (58); (3) importantly, STORM imaging reveals condensin clusters with various sizes, which are consistent with diffusion capture (58). These two DNA looping pathways could also function collaboratively through ATPase-dependent DNA loop extrusion after diffusion capture of DNA by cohesin-NIPBL. Furthermore, capturing the second DNA

segment by the arm-hinge of cohesin could contribute to the bridging of sister chromatids and cohesion. Consistent with this notion, mutations in the yeast SMC1 and SMC3 hinge domains that neutralize a positively charged channel led to sister chromatin cohesion defects (59).

Despite recent experimental demonstrations of DNA loop extrusion by cohesin and condensin *in vitro* and *in cellulo* (22, 23, 25, 47, 60–63), we have not reached a consensus regarding the molecular mechanism of DNA loop extrusion (36). HS-AFM imaging in this study demonstrates that once DNA is bound to the globular domain in the DNA "gripping/clamping" state (25), the SMC arm-hinge domain of both WT and ATPase mutant cohesin^{SA1}-NIPBL^{c} is free to search and capture the next DNA fragment through arm extension (Fig. 8), leading to the initiation of a DNA loop. These results show that it is not the ATP hydrolysis or power stroke that drives arm extension and capture of the DNA segment. The conformational change of cohesin-NIPBL that drives DNA loop growth is still hotly debated. The Brownian ratchet model postulates that loop growth depends on the stochastic Brownian motion of the Scc3-hinge domain, followed by DNA slipping along the Scc2-head domain (26). The “swing” and “clamp” model posits that DNA translocation and loop growth is through the synchronization of the head-disengagement/engagement driven by the ATPase cycle and arm-hinge swing/DNA clamping (25). While HS-AFM imaging does not provide detail on relative movements of the SMC head domains, SA1, and NIPBL during DNA loop extrusion, it shows DNA loop extrusion with cohesin^{SA1}-NIPBL^{c} partially anchored to a surface. This result suggests a mechanism that relies on cohesin-NIPBL switching between DNA gripping and slipping states where DNA can slide across the cohesin-NIPBL globular domain/lower compartment, leading to DNA loop growth.

It is known that tension on DNA reduces the DNA loop extrusion step size (48). Consistent with this notion, in HS-AFM imaging, since DNA was partially anchored onto a surface that likely generates tension, we observed "bursts" of DNA loop extrusion events when the tension on DNA was favorable. Consistent with the presence of tension on DNA, the DNA looping step size measured from HS-AFM images (∼13 nm or 42 bp) is considerably lower than what is estimated by combining the loop extrusion speed (∼0.5–1 kb/s) and ATPase rate (2 ATP/s) (22, 23). Meanwhile, it is worth noting that the DNA loop extension step size by cohesin-NIPBL measured using HS-AFM is slightly smaller than that of condensin under DNA stretching forces from 1 to 0.2 pN (∼20–40 nm) (48). In addition, HS-AFM imaging shows both forward and reserve steps, suggesting that cohesin-NIPBL can switch DNA strands during DNA loop extrusion. It is highly likely that surface anchoring of DNA and cohesin-NIPBL during HS-AFM imaging increases the frequency of strand switching and DNA loop extrusion pausing (64–72).

In summary, HS-AFM imaging reveals dynamic conformational changes of cohesin-NIPBL that drive DNA loading and loop initiation. This study uncovers critical missing links in our understanding of cohesin-NIPBL DNA binding and DNA loop extrusion (73, 74).

Experimental procedures

Protein purification

WT, SMC1A-E1157Q/SMC3-E1144Q (EQ) ATPase mutant cohesin^{SA1}-NIPBL^{c} (SA1 containing cohesin with the C-terminal HEAT repeat domain of NIPBL 1163-2804 AAs), cohesin-NIPBL^{c} without SA1, cohesin^{SA1} without NIPBL^{c}, cohesin^{SA1}-NIPBL with SA1 C-terminal truncation (SA1 1-1054 AAs, cohesin^{SA1dc}-NIPBL), cohesin^{SA1}-NIPBL with NIPBL C-terminal truncation (NIPBL 1163-2630 AAs, cohesin^{SA1}-NIPBLdc), and cohesin^{SA1dc}-NIPBLdc were purified according to the same protocols published previously (22). The full complex was formed by mixing purified subcomplex containing SMC1, SMC3, RAD21, and NIPBL subunits with separately purified SA1. Purification of full-length SA1/SA2 and SA2 fragments (1–301, 1–450, and 1052–1231 AAs) was described previously (37, 43, 44, 64).

DNA substrates

pG5E4-5S plasmid (5190 bp, a gift from the Williams lab at UNC-Chapel Hill) was linearized using NdeI restriction enzyme (NEB) and purified using the Qiagen PCR purification kit. The 45 bp duplex DNA for fluorescence anisotropy was prepared as described previously (44).

AFM imaging in air

Purified linear dsDNA (6 nM, 5190 bp) was incubated with WT or mutant cohesin^{SA1}-NIPBL^{c} (30 nM) in cohesin buffer (40 mM Tris pH 8, 50 mM NaCl, 2 mM $MgCl_2$, 1 mM DTT) either without or with ATP (2.5 mM) for 1 min at room temperature. All samples were diluted 16-fold in AFM imaging buffer (20 mM Hepes pH 7.6, 100 mM NaCl, and 10 mM Mg $(C_2H_3O_2)_2$) and immediately deposited onto a freshly cleaved mica surface. The deposited samples were washed with deionized water and dried under nitrogen gas streams before AFM imaging. AFM imaging in air was carried out using the AC mode on an MFP-3D-Bio AFM (Asylum Research, Oxford Instruments) with Pointprobe PPP-FMR probes (Nanosensors, spring constants at ∼2.8 N/m). All images were captured at scan sizes of 1 × 1 μm^2 to 3 × 3 μm^2, a scan rate of 1 to 2 Hz, and a resolution of 512 × 512 pixels. AFM images were first flattened to first order polynomial. Protein binding positions on DNA were measured using the “Section” function in the “Analyze Panel” in the Asylum Research AFM (https://support.asylumresearch.com/articles/software-downloads) software. DNA bending angle analysis was done using Image J (https://imagej.nih.gov/ij/download.html) software. Volume Analysis was done using the Particle Analysis module in the Asylum Research AFM (https://support.asylumresearch.com/articles/software-downloads) software. All particles in the edge of AFM images were ignored for analysis.

HS-AFM imaging in liquids

WT or ATPase mutant cohesin^{SA1}-NIPBL^{c} (30 nM) was incubated with the linear dsDNA substrate (3 nM) in cohesin buffer for 1 min at room temperature, followed by a 1 min incubation with ATP (4 mM). The incubated sample was diluted 20-fold in cohesin buffer and deposited onto a freshly prepared APS-treated mica surface (45). APS was synthesized in-house to ensure high purity (a gift from the Erie lab at UNC-Chapel Hill), using a protocol provided by the Lyubchenko group (University of Nebraska). The protein-DNA sample was further incubated on the APS-mica surface for 2 min, followed by washing with cohesin buffer (500 μl). The washed sample was scanned in cohesin buffer containing ATP on either a Cypher VRS AFM (Asylum Research) using BioLever fast (AC10DS) cantilevers or JPK NanoWizard 4 using USC-F0.3-k0.3 cantilevers. For Cypher VRS, we used BlueDrive Photothermal Excitation to drive the cantilever. The images were scanned at 0.4 to 2.3 frames/s.

All high-speed AFM data from Cypher VRS and JPK systems were analyzed using Asylum or JPK image analysis software, respectively. Movies were separated into individual frames using the Asylum and JPK image analysis software. The DNA loop lengths and cohesin arm extension were measured by tracing the DNA or arm using the "Analyze Panel" in Asylum MFP3D software through cross-section analysis or through tracing the molecules using Image J software for images collected on JPK. Arm extension and DNA loop extrusion step size were calculated based on the SMC arm or DNA loop length changes between consecutive HS-AFM image frames.

Fluorescence anisotropy

His_6-tagged full-length SA2 and SA2 fragments in DNA-binding buffer (20 mM Hepes, pH 7.5, 0.1 mM $MgCl_2$, 0.5 mM DTT, 100 mM KCl) were titrated into the binding solution containing fluorescein-labeled DNA substrates (6 nM, 45 bp) using a Tecan Spark Multimode plate reader (Tecan Group Ltd) (64). The data obtained from fluorescence anisotropy were analyzed by using the equation $P = ((P_{bound}-P_{free})[protein]/(Kd + [protein])) + P_{free}$, where P is the polarization measured at a given total protein concentration, P_{free} is the initial polarization of fluorescein-labeled DNA without protein binding, P_{bound} is the maximum polarization of DNA due to binding of proteins, and [protein] is the total protein concentration. The average equilibrium dissociation constant (K_d) was based on three measurements.

Statistical analysis

All WT and mutant cohesin data were from two to three independent protein preparations. Data from AFM imaging in air were pooled from at least two to three independent experiments. HS-AFM in liquids data were from multiple sample depositions (5 for WT and 2 for EQ mutant). Arm extension and loop extrusion step sizes were analyzed from 18 videos and 611 image frames. Statistical analysis was carried out using OriginPro (OriginLab). Unless stated otherwise, the error bars represent SD. The p-value was calculated by Student's t test, and the statistically significant level was set at $p < 0.05$.

Data availability

All data within the article will be shared upon request (corresponding authors).

Supporting information—This article contains supporting information (41).

Acknowledgments—We would like to thank Ryan Fuierer and Keith Jones at Asylum Research and Dorothy Erie at the University of North Carolina at Chapel Hill for access to HS-AFM and technical support.

Author contributions—P. K., H. Z., I. J. F., Y. J. T., H. Y., and H. W. conceptualization; P. K., X. L., Q. X., E. M. I., C. P., and Z. S. data curation; P. K. methodology; P. K., X. L., Q. X., E. M. I., C. P., and Z. S. formal analysis; H. Z., I. J. F., Y. J. T., H. Y., and H. W. supervision; H. Z., I. J. F., Y. J. T., H. Y., and H. W. writing–original draft; H. Z., I. J. F., Y. J. T., H. Y., and H. W. writing–review and editing.

Funding and additional information—This work was supported by the National Institutes of Health [P01CA092584 to I. J. F.], Welch Foundation [C-1565 to Y. J. T. and F-1808 to I. J. F.], National Natural Science Foundation of China [Projects 32271264 to Z. S. and 32130053 to H. Y.], and Westlake Education Foundation [to Z. S. and H. Y.]

Conflict of interest—The authors declare that they have no conflicts of interest with the contents of this article.Figure Legends

Abbreviations—The abbreviations used are: APS, 1-(3-Aminopropyl)silatrane; HS-AFM, high-speed atomic force microscopy; SMC, structural maintenance of chromosome; TAD, topologically associating domain.

References

1. Lieberman-Aiden, E., van Berkum, N. L., Williams, L., Imakaev, M., Ragoczy, T., Telling, A., *et al.* (2009) Comprehensive mapping of long-range interactions reveals folding principles of the human genome. *Science* **326**, 289–293
2. Dixon, J. R., Selvaraj, S., Yue, F., Kim, A., Li, Y., Shen, Y., *et al.* (2012) Topological domains in mammalian genomes identified by analysis of chromatin interactions. *Nature* **485**, 376–380
3. Nora, E. P., Lajoie, B. R., Schulz, E. G., Giorgetti, L., Okamoto, I., Servant, N., *et al.* (2012) Spatial partitioning of the regulatory landscape of the X-inactivation centre. *Nature* **485**, 381–385
4. Sexton, T., Yaffe, E., Kenigsberg, E., Bantignies, F., Leblanc, B., Hoichman, M., *et al.* (2012) Three-dimensional folding and functional organization principles of the Drosophila genome. *Cell* **148**, 458–472
5. Rao, S. S., Huntley, M. H., Durand, N. C., Stamenova, E. K., Bochkov, I. D., Robinson, J. T., *et al.* (2014) A 3D map of the human genome at kilobase resolution reveals principles of chromatin looping. *Cell* **159**, 1665–1680
6. Pope, B. D., Ryba, T., Dileep, V., Yue, F., Wu, W., Denas, O., *et al.* (2014) Topologically associating domains are stable units of replication-timing regulation. *Nature* **515**, 402–405
7. Andrey, G., Montavon, T., Mascrez, B., Gonzalez, F., Noordermeer, D., Leleu, M., *et al.* (2013) A switch between topological domains underlies HoxD genes collinearity in mouse limbs. *Science* **340**, 1234167

8. Lupianez, D. G., Kraft, K., Heinrich, V., Krawitz, P., Brancati, F., Klopocki, E., *et al.* (2015) Disruptions of topological chromatin domains cause pathogenic rewiring of gene-enhancer interactions. *Cell* **161**, 1012–1025
9. Symmons, O., Uslu, V. V., Tsujimura, T., Ruf, S., Nassari, S., Schwarzer, W., *et al.* (2014) Functional and topological characteristics of mammalian regulatory domains. *Genome Res.* **24**, 390–400
10. Peters, J. M. (2021) How DNA loop extrusion mediated by cohesin enables V(D)J recombination. *Curr. Opin. Cell Biol.* **70**, 75–83
11. Merkenschlager, M., and Nora, E. P. (2016) CTCF and cohesin in genome folding and transcriptional gene regulation. *Annu. Rev. Genomics Hum. Genet.* **17**, 17–43
12. Hassler, M., Shaltiel, I. A., and Haering, C. H. (2018) Towards a unified model of SMC complex function. *Curr. Biol.* **28**, R1266–R1281
13. Yatskevich, S., Rhodes, J., and Nasmyth, K. (2019) Organization of chromosomal DNA by SMC complexes. *Annu. Rev. Genet.* **53**, 445–482
14. Xiao, T., Wallace, J., and Felsenfeld, G. (2011) Specific sites in the C terminus of CTCF interact with the SA2 subunit of the cohesin complex and are required for cohesin-dependent insulation activity. *Mol. Cell. Biol.* **31**, 2174–2183
15. Nasmyth, K., and Haering, C. H. (2009) Cohesin: its roles and mechanisms. *Annu. Rev. Genet.* **43**, 525–558
16. Sofueva, S., Yaffe, E., Chan, W. C., Georgopoulou, D., Vietri Rudan, M., Mira-Bontenbal, H., *et al.* (2013) Cohesin-mediated interactions organize chromosomal domain architecture. *EMBO J.* **32**, 3119–3129
17. Guo, Y., Xu, Q., Canzio, D., Shou, J., Li, J., Gorkin, D. U., *et al.* (2015) CRISPR inversion of CTCF sites alters genome topology and enhancer/promoter function. *Cell* **162**, 900–910
18. Narendra, V., Rocha, P. P., An, D., Raviram, R., Skok, J. A., Mazzoni, E. O., *et al.* (2015) CTCF establishes discrete functional chromatin domains at the Hox clusters during differentiation. *Science* **347**, 1017–1021
19. Phillips-Cremins, J. E., Sauria, M. E., Sanyal, A., Gerasimova, T. I., Lajoie, B. R., Bell, J. S., *et al.* (2013) Architectural protein subclasses shape 3D organization of genomes during lineage commitment. *Cell* **153**, 1281–1295
20. Seitan, V. C., Banks, P., Laval, S., Majid, N. A., Dorsett, D., Rana, A., *et al.* (2006) Metazoan Scc4 homologs link sister chromatid cohesion to cell and axon migration guidance. *PLoS Biol.* **4**, e242
21. Zuin, J., Dixon, J. R., van der Reijden, M. I., Ye, Z., Kolovos, P., Brouwer, R. W., *et al.* (2014) Cohesin and CTCF differentially affect chromatin architecture and gene expression in human cells. *Proc. Natl. Acad. Sci. U. S. A.* **111**, 996–1001
22. Kim, Y., Shi, Z., Zhang, H., Finkelstein, I. J., and Yu, H. (2019) Human cohesin compacts DNA by loop extrusion. *Science* **366**, 1345–1349
23. Davidson, I. F., Bauer, B., Goetz, D., Tang, W., Wutz, G., and Peters, J. M. (2019) DNA loop extrusion by human cohesin. *Science* **366**, 1338–1345
24. Banigan, E. J., and Mirny, L. A. (2020) The interplay between asymmetric and symmetric DNA loop extrusion. *Elife* **9**, e63528
25. Bauer, B. W., Davidson, I. F., Canena, D., Wutz, G., Tang, W., Litos, G., *et al.* (2021) Cohesin mediates DNA loop extrusion by a "swing and clamp" mechanism. *Cell* **184**, 5448–5464.e5422
26. Higashi, T. L., Pobegalov, G., Tang, M., Molodtsov, M. I., and Uhlmann, F. (2021) A Brownian ratchet model for DNA loop extrusion by the cohesin complex. *Elife* **10**, e67530
27. Fudenberg, G., Abdennur, N., Imakaev, M., Goloborodko, A., and Mirny, L. A. (2017) Emerging evidence of chromosome folding by loop extrusion. *Cold Spring Harb. Symposia Quant. Biol.* **82**, 45–55
28. Fudenberg, G., Imakaev, M., Lu, C., Goloborodko, A., Abdennur, N., and Mirny, L. A. (2016) Formation of chromosomal domains by loop extrusion. *Cell Rep.* **15**, 2038–2049
29. Anderson, D. E., Losada, A., Erickson, H. P., and Hirano, T. (2002) Condensin and cohesin display different arm conformations with characteristic hinge angles. *J. Cell Biol.* **156**, 419–424
30. Eeftens, J. M., Katan, A. J., Kschonsak, M., Hassler, M., de Wilde, L., Dief, E. M., *et al.* (2016) Condensin Smc2-Smc4 dimers are flexible and dynamic. *Cell Rep.* **14**, 1813–1818
31. Sedeno Cacciatore, A., and Rowland, B. D. (2019) Loop formation by SMC complexes: turning heads, bending elbows, and fixed anchors. *Curr. Opin. Genet. Dev.* **55**, 11–18
32. Burmann, F., Lee, B. G., Than, T., Sinn, L., O'Reilly, F. J., Yatskevich, S., *et al.* (2019) A folded conformation of MukBEF and cohesin. *Nat. Struct. Mol. Biol.* **26**, 227–236
33. Ryu, J. K., Katan, A. J., van der Sluis, E. O., Wisse, T., de Groot, R., Haering, C. H., *et al.* (2020) The condensin holocomplex cycles dynamically between open and collapsed states. *Nat. Struct. Mol. Biol.* **27**, 1134–1141
34. Nichols, M. H., and Corces, V. G. (2018) A tethered-inchworm model of SMC DNA translocation. *Nat. Struct. Mol. Biol.* **25**, 906–910
35. Marko, J. F., De Los Rios, P., Barducci, A., and Gruber, S. (2019) DNA-segment-capture model for loop extrusion by structural maintenance of chromosome (SMC) protein complexes. *Nucleic Acids Res.* **47**, 6956–6972
36. Higashi, T. L., and Uhlmann, F. (2022) SMC complexes: lifting the lid on loop extrusion. *Curr. Opin. Cell Biol.* **74**, 13–22
37. Lin, J., Countryman, P., Chen, H., Pan, H., Fan, Y., Jiang, Y., *et al.* (2016) Functional interplay between SA1 and TRF1 in telomeric DNA binding and DNA-DNA pairing. *Nucleic Acids Res.* **44**, 6363–6376
38. Shi, Z., Gao, H., Bai, X. C., and Yu, H. (2020) Cryo-EM structure of the human cohesin-NIPBL-DNA complex. *Science* **368**, 1454–1459
39. Ando, T. (2019) High-speed atomic force microscopy. *Curr. Opin. Chem. Biol.* **51**, 105–112
40. Collier, J. E., and Nasmyth, K. A. (2022) DNA passes through cohesin's hinge as well as its Smc3-kleisin interface. *Elife* **11**, e80310
41. Kaur, P., Wu, D., Lin, J., Countryman, P., Bradford, K. C., Erie, D. A., *et al.* (2016) Enhanced electrostatic force microscopy reveals higher-order DNA looping mediated by the telomeric protein TRF2. *Sci. Rep.* **6**, 20513
42. Kong, X., Ball, A. R., Jr., Pham, H. X., Zeng, W., Chen, H. Y., Schmiesing, J. A., *et al.* (2014) Distinct functions of human cohesin-SA1 and cohesin-SA2 in double-strand break repair. *Mol. Cell. Biol.* **34**, 685–698
43. Zhang, N., Jiang, Y., Mao, Q., Demeler, B., Tao, Y. J., and Pati, D. (2013) Characterization of the interaction between the cohesin subunits Rad21 and SA1/2. *PLoS one* **8**, e69458
44. Countryman, P., Fan, Y., Gorthi, A., Pan, H., Strickland, J., Kaur, P., *et al.* (2018) Cohesin SA2 is a sequence-independent DNA-binding protein that recognizes DNA replication and repair intermediates. *J. Biol. Chem.* **293**, 1054–1069
45. Shlyakhtenko, L. S., Gall, A. A., and Lyubchenko, Y. L. (2013) Mica functionalization for imaging of DNA and protein-DNA complexes with atomic force microscopy. *Methods Mol. Biol.* **931**, 295–312
46. Li, Z., Kaur, P., Lo, C. Y., Chopra, N., Smith, J., Wang, H., *et al.* (2022) Structural and dynamic basis of DNA capture and translocation by mitochondrial Twinkle helicase. *Nucleic Acids Res.* **50**, 11965–11978
47. Kim, E., Kerssemakers, J., Shaltiel, I. A., Haering, C. H., and Dekker, C. (2020) DNA-loop extruding condensin complexes can traverse one another. *Nature* **579**, 438–442
48. Ryu, J. K., Rah, S. H., Janissen, R., Kerssemakers, J. W. J., Bonato, A., Michieletto, D., *et al.* (2022) Condensin extrudes DNA loops in steps up to hundreds of base pairs that are generated by ATP binding events. *Nucleic Acids Res.* **50**, 820–832
49. Gruber, S., Arumugam, P., Katou, Y., Kuglitsch, D., Helmhart, W., Shirahige, K., *et al.* (2006) Evidence that loading of cohesin onto chromosomes involves opening of its SMC hinge. *Cell* **127**, 523–537
50. Buheitel, J., and Stemmann, O. (2013) Prophase pathway-dependent removal of cohesin from human chromosomes requires opening of the Smc3-Scc1 gate. *EMBO J.* **32**, 666–676
51. Higashi, T. L., Eickhoff, P., Sousa, J. S., Locke, J., Nans, A., Flynn, H. R., *et al.* (2020) A structure-based mechanism for DNA entry into the cohesin ring. *Mol. Cell* **79**, 917–933.e919
52. Shaltiel, I. A., Datta, S., Lecomte, L., Hassler, M., Kschonsak, M., Bravo, S., *et al.* (2022) A hold-and-feed mechanism drives directional DNA loop extrusion by condensin. *Science* **376**, 1087–1094
53. Srinivasan, M., Scheinost, J. C., Petela, N. J., Gligoris, T. G., Wissler, M., Ogushi, S., *et al.* (2018) The cohesin ring uses its hinge to organize DNA using Non-topological as well as topological mechanisms. *Cell* **173**, 1508–1519.e1518

54. Hinckley, D. M., Freeman, G. S., Whitmer, J. K., and de Pablo, J. J. (2013) An experimentally-informed coarse-grained 3-Site-Per-Nucleotide model of DNA: structure, thermodynamics, and dynamics of hybridization. *J. Chem. Phys.* **139**, 144903
55. Tan, C., Jung, J., Kobayashi, C., Torre, D. U., Takada, S., and Sugita, Y. (2022) Implementation of residue-level coarse-grained models in GENESIS for large-scale molecular dynamics simulations. *PLoS Comput. Biol.* **18**, e1009578
56. Liu, S., Lin, X., and Zhang, B. (2022) Chromatin fiber breaks into clutches under tension and crowding. *Nucleic Acids Res.* **50**, 9738–9747
57. Rao, S. S. P., Huang, S. C., Glenn St Hilaire, B., Engreitz, J. M., Perez, E. M., Kieffer-Kwon, K. R., *et al.* (2017) Cohesin loss eliminates all loop domains. *Cell* **171**, 305–320.e324
58. Gerguri, T., Fu, X., Kakui, Y., Khatri, B. S., Barrington, C., Bates, P. A., *et al.* (2021) Comparison of loop extrusion and diffusion capture as mitotic chromosome formation pathways in fission yeast. *Nucleic Acids Res.* **49**, 1294–1312
59. Kurze, A., Michie, K. A., Dixon, S. E., Mishra, A., Itoh, T., Khalid, S., *et al.* (2011) A positively charged channel within the Smc1/Smc3 hinge required for sister chromatid cohesion. *EMBO J.* **30**, 364–378
60. [preprint] Beckwith, K., Odegard-Fougner, O., Morero, N., Barton, C., Schueder, F., Alexander, S., *et al.* (2021) Visualization of loop extrusion by DNA nanoscale tracing in single human cell. *bioRxiv*. https://doi.org/10.1101/2021.04.12.439407
61. Ganji, M., Shaltiel, I. A., Bisht, S., Kim, E., Kalichava, A., Haering, C. H., *et al.* (2018) Real-time imaging of DNA loop extrusion by condensin. *Science* **360**, 102–105
62. Kong, M., Cutts, E. E., Pan, D., Beuron, F., Kaliyappan, T., Xue, C., *et al.* (2020) Human condensin I and II drive extensive ATP-dependent compaction of nucleosome-bound DNA. *Mol. Cell* **79**, 99–114.e119
63. Golfier, S., Quail, T., Kimura, H., and Brugues, J. (2020) Cohesin and condensin extrude DNA loops in a cell cycle-dependent manner. *Elife* **9**, e53885
64. Pan, H., Jin, M., Ghadiyaram, A., Kaur, P., Miller, H. E., Ta, H. M., *et al.* (2020) Cohesin SA1 and SA2 are RNA binding proteins that localize to RNA containing regions on DNA. *Nucleic Acids Res.* **48**, 5639–5655
65. Roy, D., Zhang, Z., Lu, Z., Hsieh, C. L., and Lieber, M. R. (2010) Competition between the RNA transcript and the nontemplate DNA strand during R-loop formation *in vitro*: a nick can serve as a strong R-loop initiation site. *Mol. Cell Biol.* **30**, 146–159
66. Lu, W. T., Hawley, B. R., Skalka, G. L., Baldock, R. A., Smith, E. M., Bader, A. S., *et al.* (2018) Drosha drives the formation of DNA:RNA hybrids around DNA break sites to facilitate DNA repair. *Nat. Commun.* **9**, 532
67. Cohen, S., Puget, N., Lin, Y. L., Clouaire, T., Aguirrebengoa, M., Rocher, V., *et al.* (2018) Senataxin resolves RNA:DNA hybrids forming at DNA double-strand breaks to prevent translocations. *Nat. Commun.* **9**, 533
68. Long, Q., Liu, Z., and Gullerova, M. (2021) Sweet melody or jazz? Transcription around DNA double-strand breaks. *Front. Mol. Biosci.* **8**, 655786
69. Teng, Y., Yadav, T., Duan, M., Tan, J., Xiang, Y., Gao, B., *et al.* (2018) ROS-induced R loops trigger a transcription-coupled but BRCA1/2-independent homologous recombination pathway through CSB. *Nat. Commun.* **9**, 4115
70. Ouyang, J., Yadav, T., Zhang, J. M., Yang, H., Rheinbay, E., Guo, H., *et al.* (2021) RNA transcripts stimulate homologous recombination by forming DR-loops. *Nature* **594**, 283–288
71. [preprint] Yang, J., Brandao, H. B., and Hansen, A. S. (2022) DNA double-strand break end synapsis by DNA loop extrusion. *bioRxiv*. https://doi.org/10.1038/s41467-023-37583-w
72. Lebraud, E., Pinna, G., Siberchicot, C., Depagne, J., Busso, D., Fantini, D., *et al.* (2020) Chromatin recruitment of OGG1 requires cohesin and mediator and is essential for efficient 8-oxoG removal. *Nucleic Acids Res.* **48**, 9082–9097
73. Marnef, A., and Legube, G. (2021) R-loops as Janus-faced modulators of DNA repair. *Nat. Cell Biol.* **23**, 305–313
74. Yasuhara, T., and Zou, L. (2021) Impacts of chromatin dynamics and compartmentalization on DNA repair. *DNA Repair* **105**, 103162